Glass Europe Vol. 4 (2026) 63-83
https://doi.org/10.52825/glass-europe.v4i.1139

Submitted: 25 Feb. 2024 | Accepted: 31 Dec. 2024 | 08 May 2026

Role of Iron on Properties of Calcium Aluminate Glasses and Melts

Rawan El Hayek[1,2], Frédérique Ferey[2], Alexander Pisch[2,$], Maria Rita Cicconi[1,#], Delphine Vantelon[3], and Daniel R. Neuville[1,*]

[1]Geomat Lab, IPGP-CNRS, Université de Paris, 1 rue Jussieu, 75005 Paris, France

[2]Holcim Innovation Center, 95 Rue de Montmurier,38070 Saint Quentin Fallavier, France

[3]SOLEIL, L'orme des merisiers, St Aubin, 91000.

[$]Present address: University Grenoble Alpes, Laboratoire SIMaP, 38000 Grenoble, France

[#]Present address: Friedrich-Alexander-Universität Erlangen-Nürnberg, Department of Materials Science and Engineering, Institut für Glas und Keramik, Martensstrasse 5, 91058, Erlangen, Germany

*Correspondance: Daniel R. Neuville, neuville@ipgp.fr

Abstract. $CaO-Al_2O_3$ based glasses are studied due to their presence in hydraulic binders/refractory cements. With the addition of Fe, an increased complexity in the phase diagrams and the liquid structure is observed as this element can exist in two different oxidation states which plays different roles in a liquid/glass matrix.

The aim of this study is to understand the influence iron addition in a $CaO-Al_2O_3-B_2O_3$ glass. B_2O_3 was added to simulate a liquid phase present in some Belite-Ye'elimite-Ferrite clinkers in which a glassy phase is observed. Iron is mainly present in the Fe^{3+} form in four-fold coordination. Viscosity and glass transition temperatures decrease with the addition of Fe_2O_3 which has an important impact for the clinkering process. This decrease with iron correlates with the appearance of a new band at 650 cm^{-1} in the Raman spectrum which can be assigned to the vibration of Al—O—$^{[4]}Fe^{3+}$—O—Al links.

Keywords: Invert Glasses, Aluminate, Melt, Structure, Viscosity, Clinker

1. Introduction

The $CaO-Al_2O_3-SiO_2$ ternary diagram is particularly important for earth and materials sciences (E glass, acid or basic slag, Portland cement, high alumina cement...). One of the key challenges of the energy transition is to reduce CO_2 emissions in the manufacture of materials, particularly cement. The cement industry significantly contributes to climate change as it is responsible for 7% of global anthropogenic CO_2 emissions [1]. The total cement production averaged about 4100 Mt/year worldwide between 2014 and 2019 and is expected to remain stable [1]. Hence, there is great interest in developing new hydraulic clinkers that produce a lower carbon footprint both to prevent the associated environmental impacts and to avoid the costs of CO_2 taxes that are likely to increase in the future. Recently, the growing interest of glassy materials used as secondary cementitious materials in blended cements led to new studies relating the glass properties to their performance in final cements [2]. The thermodynamic and physico-chemical properties of the glass were related to their hydration reactivity, but the behavior is not fully quantitatively understood due to the missing relation between fundamental thermodynamic properties and the local structure in the glass.

Iron oxide is one of the major components in low CO_2 BYF-type cements [3], [4], [5], [6] as well as in Ordinary Portland Cements (OPC) and calcium aluminate cements. In the BYF clinker production, a C-A-F liquid phase controls / influences the formation and properties of ye'elimite – the key active component [7]. The structure of the molten calcium-aluminate phases in cement comprises interpenetrating CaO and Al_2O_3 rich phases that closely resemble the corresponding crystals [8]. In OPC clinkers, the addition of Fe_2O_3 in combination with CaO and Al_2O_3 lowers the melting point from 1430 ºC to 1339 ºC in the sintering zone of the rotary kiln [9]. This is the origin of the common understanding in the cement manufacturing industry that an increase of the iron oxide content in the raw mix increases the amount of liquid phase and therefore decreases the maximum clinker burning temperature in the sintering zone of the rotary kiln. However, the underlying thermodynamics of this process is not fully understood [10], [11]. The maximum amount of liquid phase at a given temperature is predicted from a phase diagram point of view for an A/F ratio of 1.38 [11]. The observed increase in the raw mix burnability in high iron bearing raw mixes must therefore have additional causes beyond the decrease of the melting temperature.

The burnability of a raw mix is influenced by its particle size distribution, which depends mostly on the grain size of silica and the viscosity of the liquid phase formed during clinkerization [10]. The viscosity of this liquid phase remains largely unknown, as Fe-bearing compositions are hard to vitrify and often crystallize. Timashev [12] and Butt et al. [13] claimed that additional electronegative elements decrease the viscosity by changing the distribution between Al^{3+}/Fe^{3+} in octahedral or tetrahedral coordination. However, this does not explain why a higher burnability is also observed in the pure quaternary CaO-SiO_2-Al_2O_3-Fe_2O_3 system. The current insight comes mostly from experiments on silicate and aluminosilicate systems, but data on calcium aluminate systems is scarce. The viscosity of aluminosilicate melts decreases by more than an order of magnitude after substituting Si^{4+} or Al^{3+} by Fe^{3+} [14], [15], [16], [17]. The viscosity of aluminosilicates and ferrosilicates of the same stoichiometry diminishes when Al^{3+} is replaced by Fe^{3+} as the energy of the Fe-O bond is lower than that of the Al-O bond which weakens the system [17].

Several studies contributed to the basic understanding of redox reactions [18], [19], [20], [21], [22], [23] and concluded that these reactions are dominated by diffusional mechanisms [22]. Nevertheless, the exact nature of the implied species involved in the redox reactions is still a topic of numerous debates: O_2, O^{2-}, divalent or monovalent cations and it seems also to be temperature dependent [23], [24], [25], [26], [27]. This is partly due to the fact that the conditions of temperature, oxygen partial pressure and chemical composition that govern the redox mechanism remain partially unconstrained. Some authors showed that the iron oxidation / reduction reactions near the glass transition temperature T_g in dry iron-aluminosilicate glasses [22], [28], [29], Fe-bearing pyroxene or Fe-borosilicate glasses [23], [30], [31], [32] could be controlled by the migration of divalent cations (Ca^{2+}, Mg^{2+}, Fe^{2+}) through a crystallized layer formed at the surface. The migration of these ions is charge-balanced by a counter flow of electron holes [23].

Calcium aluminate glasses are an analogous of the C-A-F liquid formed during the synthesis of OPC and BYF clinkers. Their structures show great variability in their local aluminium and calcium environments depending on the Al_2O_3 / CaO ratio. Al is essentially in 4-fold coordination. Tetrahedral aluminium may be present as Q^2, Q^3 or Q^4 species as a function of the Al_2O_3 / CaO ratio (Q^n indicates tetrahedral sites with n bridging oxygen) [33], [34], [35], [36], [37]. Meanwhile calcium, playing the role of a charge compensator, may exist in six-fold coordination in a depolymerized system like the C_3A glass or in 7-fold coordination in a more polymerized one as the CA glass [33], [34], [38], [39], [40], [41], [42], [43], [44]. The interest in calcium aluminosilicate glasses includes applications in cement production [7], [10], glass industry [45], and fundamental research because they correspond to the so-called "invert glasses" ([Network modifiers] > [Network Formers]).

The presence of boron oxide in the raw mix reduces the formation temperature of the liquid phase [46], [47] and plays a role in the activation of pseudo-cubic ye'elimite during clinkering [48]. The relationship between the origin of this amorphous phase, its macroscopic properties and the concentration / redox of iron in the slag was never studied in spite of the fact that the burning conditions may change the valence of this element. At low concentrations (< 2 mol%), boron causes the formation of BO_3 units in Ca-aluminate glasses, resulting in a drop of Tg and the temperature of formation of the liquid phase [37]. Boron and aluminium do not mix randomly in Ca-aluminate glasses, creating two subnetworks at higher boron contents and increasing viscosity [37].

The aim of this contribution is to investigate the effect of iron in the structure and properties of calcium aluminoborate glasses that approximate the composition of the liquid phase formed during the production of a BYF clinker. Several glasses based on the composition CAB35.02 (with 35 mol% Al_2O_3, 2 mol% B_2O_3 and the complement CaO) investigated by El-Hayek et al [37] were doped with iron. In the present study, the redox state of iron and its local environment were investigated using wet chemical analysis, XAS spectroscopy at the Fe K-edge, and Raman spectroscopy. Densities, glass transition temperatures and viscosities at low temperature were determined in order to link the macroscopic changes to the glass structure at the nanoscale.

2. Experimental Methods

2.1 Starting Materials

Pure oxides were dried for 24 hours at: 1100°C for Al_2O_3, 550°C for $CaCO_3$ and Fe_2O_3 and 110°C for $CaB_2O_4.2H_2O$ respectively. 100g of Al_2O_3-Fe_2O_3-$CaB_2O_4.2H_2O$-$CaCO_3$ mixed powder was ground in an agate mortar with ethanol for 30 minutes. All samples have 2 mol% B_2O_3 with a fixed molar ratio of R= $CaO/(Al_2O_3+B_2O_3)$ = 1.71. The raw mix was calcined at 950°C for one hour to release CO_2. The mixture was then heated in air above liquidus temperature for 30 minutes. Glasses were obtained by dipping the bottom of the crucible in water. The melting-grinding procedure was repeated 4 times to ensure the homogeneity of each glass. X-Ray Diffraction scans and Raman spectra did not show any crystallization peaks.

The composition of each glass is reported in Table 1. The glasses were named CAFX.Y., with X indicating the molar percentage of Al_2O_3 and Y the molar percentage of Fe_2O_3 with 2 mol% of B_2O_3 and 100-(X+Y+2) indicating the molar percent of CaO. The chemical composition of each glass was measured by X-ray Fluorescence (XRF) and Inductively Coupled Plasma Atomic Emission Spectroscopy (ICP-AES) The density of the glasses was determined with the Archimedean method using toluene as an immersion liquid. The glass transition temperatures (Tg) were measured by Differential Scanning Calorimetry (DSC) in a Setaram Labsys calorimeter calibrated for temperature using the melting points and polymorphic transitions of NaCl, KCl, K_2SO_4 and CaF_2 at a heating rate of 10K/min. The reported Tg_{DSC} value is taken at the midpoint of the temperature range bound by the tangents to the two flat regions on the heat flow curves.

Table 1. *Chemical composition, in wt. %, Archimedean density, and Tg determined by DSC measurements (heating rate 10K/min). Uncertainties are given in brackets.*

Glasses	%CaO	%Al2O3	%B2O3	%Fe2O3	Density	TgDSC(K)
CAF37.00	48.8(0.9)	51.2(1.0)	0.0	0.0	2.909(5)	1117.5
CAF35.00	52.1(1.0)	46.2(0.9)	1.7(0.0)	0.0	2.907(3)	1087.0
CAF35.02	46.5(0.9)	47.8(0.9)	1.6(0.0)	3.9(0.0)	2.940(4)	1091.4
CAF33.04	45.7(0.9)	44.3((0.9)	1.8(0.0)	8.7(0.2)	2.987(2)	1060.6
CAF32.08	41.8(0.8)	40.5(0.8)	1.6(0.0)	16.7(0.3)	3.067(5)	1033.9
CAF31.12	37.2(0.7)	38.0(0.8)	1.8(0.0)	23.5(0.5)	3.160(5)	1018.9
CAF28.16	34.7(0.7)	33.3(0.7)	1.5(0.0)	30.2(0.6)	3.232(4)	991.2

2.2 Wet chemical analysis

The glass samples were dissolved in an HCl aqueous solution. Phosphoric acid was added to reduce the electrode potential for the Fe^{3+} -> Fe^{2+} reaction by stabilizing the ferric ion as a $FePO_4$ complex.

A standard solution of potassium dichromate ($K_2Cr_2O_7$) was used to determine the concentration of Fe^{2+} in the samples. 1 mole of $Cr_2O_7^{2-}$ (the oxidizing agent) reacts with 6 moles of Fe^{2+} (the reducing agent) to form 6 moles of Fe^{3+} and 2 moles of Cr^{3+}. Thus, in net ionic form:

$$Cr_2O_7^{2-} + 6Fe^{2+} + 14H^+ \rightarrow 6Fe^{3+} + 2Cr^{3+} + 7H_2O \quad (1)$$

Diphenylamine was used as an indicator to detect the end of the titration as the solution shifted from colorless to an intense purple color.

2.3 XANES

Fe K-edge X-ray absorption spectroscopy (XAS) data were collected at LUCIA beamline [49] of SOLEIL Synchrotron (France) in the range of 7000-7400 eV. The energy was calibrated setting the first inflection point of a metallic Fe foil at 7112 eV. XANES (X-Ray Absorption Near Edge Structure) spectra were reduced by background subtraction with a linear function and then normalized for atomic absorption on the average absorption coefficient of the spectral region from 7170 to 7300 eV. A particular attention was given to the analysis of the pre-edge peak, which is due to the *s*-*d* electronic transition that, although forbidden, becomes partially allowed due to the mixing of the *d*-state of the transition metal and the *p*-state of the surrounding oxygens [50]. The pre-edge peak intensity and energy position are highly sensitive to both the Fe oxidation state and its coordination [51], [52], [53]. In this study, the pre-edge peak analysis was carried out following the procedure reported in detail in [54], [55]. The background was subtracted using an arc-tangent function, and then the peak was fitted by a sum of pseudo-Voigt, pV, functions, constrained to have the same full-width half maximum (FWHM) and Lorentzian coefficient. The centroid position of the pre-edge peak represents the energy position of the de-convoluted components weighted by their integrated area.

2.4 Raman spectroscopy

Unpolarized Raman spectra were recorded at room temperature using a T64000 Jobin-Yvon® triple spectrometer equipped with a confocal system, a CCD (Charge-Coupled Detector) cooled by liquid nitrogen and an Olympus® microscope. An Ar+ laser at 488.01 nm was used as exciting source operating at 100 mW on the sample. All spectra were recorded between 40 and 2000 cm-1 with an integration time of 300s. A linear baseline was fitted directly to the Raman spectra [56]. Spectra were normalized to the total area, after baseline subtraction, and deconvoluted using the Fityk® software.

2.5 Low Temperature Viscosity measurements

Viscosity measurements on supercooled liquids were carried out in air, using the creep apparatus [57]. We used a silver cylinder attached to the upper piston to minimize the temperature gradient along the sample. The temperature was measured with two Pt-Pt/Rh10% thermocouples on the top and the bottom of the sample. The temperature difference along the cylinder was found to be less than 0.1 K. The samples used for the measurement are cylindrical, with 5 mm diameter, 10 mm height and an approximate weight of 0.5 g. By comparing with the reported values of relaxed viscosity on SRM 710 glass from the National Bureau of Standards, Neuville [57] estimate the viscosity uncertainty and the reproducibility to be less than 0.02 log units with this technique. Each point in the η *versus 1/T* curves corresponds to an average of 20-30 measurements made at different stress, which implies a Newtonian behavior characteristic of a homogeneous glass sample. The stress range varies between 6.6 to 8.7 log Nm^{-2}.

3. Results

3.1 Redox, density and molar volume

Tables 1 and 2 summarizes the chemical composition, density and the redox ratio Fe^{3+}/Fe_{tot} determined by wet chemical analysis. The redox ratio around to 0.95(±0.05) for all glass compositions. XANES spectra at the Fe K-edge are plotted on Figure 1a. The main resonance and the pre-edge regions are similar for all spectra. The pre-edge is very intense and is centered around 7114 eV. The white line is at 7132 eV and the first EXAFS oscillation is at 7200 eV. In order to get more details about Fe speciation, we focused on treatment of the pre-edge peak following Cicconi et al. [41]. Indeed, all samples show well-defined pre-edge peaks, with the strongest contributions arising from the component at 7114.4 eV (Figure 1a,b). For each glass, the background subtracted pre-edge peaks were fitted using two pseudo-Voigt functions located around 7112.65 and 7114.4 eV, in agreement with trivalent iron model compounds. Related XAS spectra and the pre-edge peaks, indicate the prevalent presence of Fe^{3+} in all glasses (Figures 1a,b). The resulting integrated intensities of the pre-edge peaks and their centroid energies (Table 2) are plotted in Figure 1c. This variogram is based on the original work of Wilke et al [52], and modified by several authors [54], [58 and references therein]. The analysis of several Fe model compounds defined some characteristic areas (shadowed ellipses in Fig 1c). This study showed that all divalent Fe model compounds have centroid energies centered around 0.9 eV above the Fe metallic edge. On the other hand, trivalent model compounds are centered at energies close to 2.4 eV [49], [52], [54]. The relative energy is plotted in reference to the first maximum of the first derivative of a metallic Fe spectrum (7112 eV). The accuracy of XANES redox measurements is explained, discussed and compared in a recent paper [53]. At constant energy, the integrated intensity of the pre-edge peaks observed in model compounds varies depending on the Fe coordination geometry [30], [51], [52], [53], [54], [59].

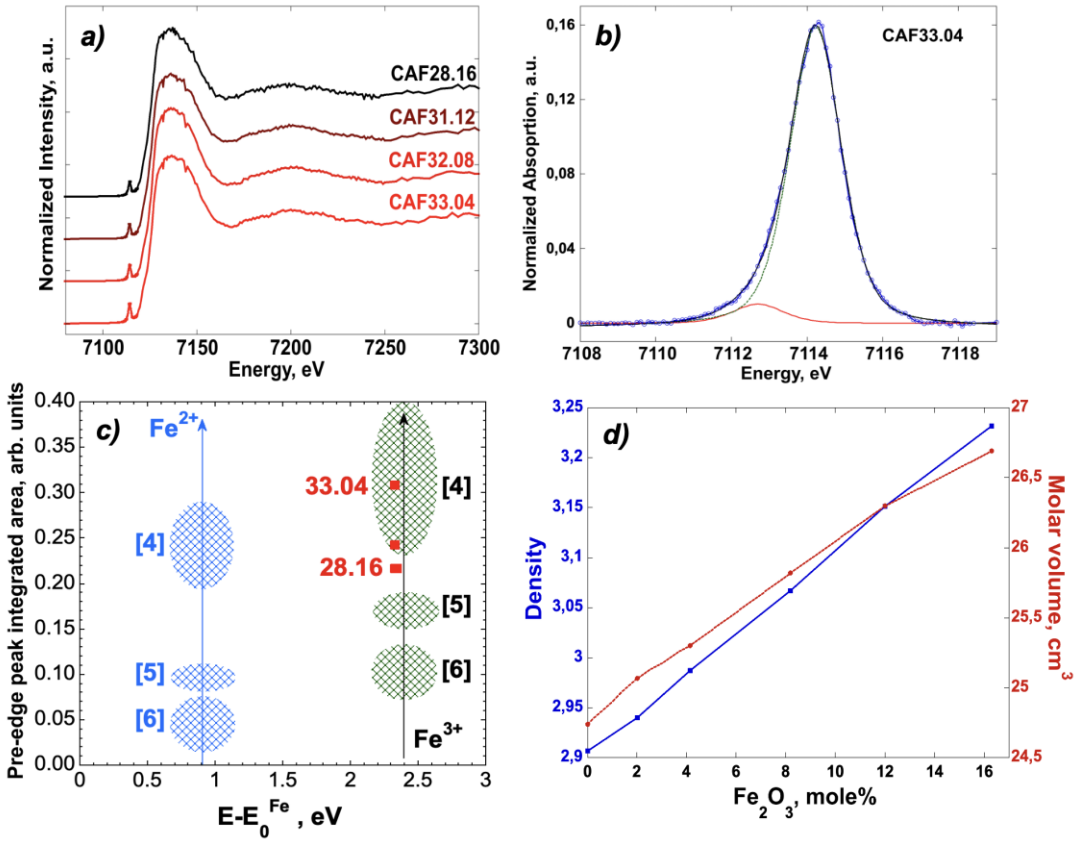

Figure 1. *a) XAS spectra of the four CAF glasses. From the top to the bottom, the amount of Fe decreases. b) Pre-edge peak region after background subtraction, for glass CAF33.04. The pre-edge peak has been deconvoluted using two pseudo-Voigt functions (dotted lines). c) Plot of the pre-edge peak integrated intensity vs. centroid energy position. Red squares refer to the CAF glasses. d) glass density versus Fe_2O_3 content in mole %.*

The pre-edge peak results are compatible with the main presence of four-coordinated $^{[4]}Fe^{3+}$ as indicated by the wet chemical analysis even if it is interesting to observe that glasses with the highest amount of Fe (i.e. CAF31.12 and CAF28.16) have lower integrated intensities (see Table 2). Indeed, while the redox state of iron does not change much, the intensity of the pre-edge peak decreases with increasing total iron content (Figure 1c). Since the integrated intensities of the Fe pre-edge peaks can also provide information on the average Fe coordination number, the de-convoluted signals in this study suggest that ferric ion is mainly four-fold coordinated for a total iron amount below 10 mol%, whereas, for higher contents, the average coordination seems to increase.

Table 2. *Calculated Centroid and Integrated experimental intensity of four CAF glasses and Fe^{3+}/Fe_{tot} determination from XANES data analysis and Wet chemistry.*

Glass	**Centroid (eV)[a]**	**Integrated intensity (a.u.)**	**Fe^{3+}/Fe_{tot}**	
			XANES	Wet Chemistry
CAF33.04	2.329	0.31	0.94(5)	0.96
CAF32.08	2.330	0.24	0.94(5)	0.95
CAF31.12	2.331	0.22	0.96(5)	0.93
CAF28.16	2.343	0.22	0.95(5)	0.94
[a]Centroid = Pre-edge peak centroid energy – 7112.0 eV (metallic foil energy)				

The XANES at Fe K-edge and the wet chemical analysis are in good agreement and confirm that iron in aluminate glasses are in a 3+ oxidation state and four-fold coordination. The addition of Fe^{3+} increases the density of the glasses (Figure 1d). Moreover, XANES spectra show clear features for glass spectra and not for a mixture of glass and crystal, which would give results corresponding to a combination of signals from pure poles, as shown recently [53].

3.2 Raman spectroscopy

Raman spectra are presented in Figure 2. The spectra can be separated in three frequency regions: the boson region between 40 – 200 cm^{-1}, the intermediate frequency region between 200 – 1100 cm^{-1} and the high frequency region between 1100 – 1800 cm^{-1}.

- *The boson region: 40-200 cm^{-1}*, the boson peak around 90 cm^{-1} is ascribed to the rotational motion of interconnected tetrahedra in glasses [60], [61], [62], [63]. The changes of the frequency and the shape of the boson peak reveal some structural changes at the medium range order. In silicate glasses for example, the boson peak shifts to higher frequencies and increases in intensity with the distortion of SiO_4 tetrahedra [62], [63]. In aluminate glasses, Al plays the same role as Si in a tetrahedral position [34], [37]. When B replaces Al, an increase in intensity and a shift of the boson peak is observed. This variation is attributed to an evolution of the network from a tetrahedral to a more triangular one following Simon et al. [64]. In our case, the boson peak shifts from 98 to 86 cm^{-1} with 12% of Fe_2O_3. This shift with the addition of Fe^{3+} is expected to be due to the replacement of Al by Fe in the same tetrahedral position due to a mass effect. For glass compositions with higher iron contents the boson peak is hidden by the Rayleigh excitation which is assigned to the nucleation of some nano-particles as already shown by several authors [65], [66], [67].

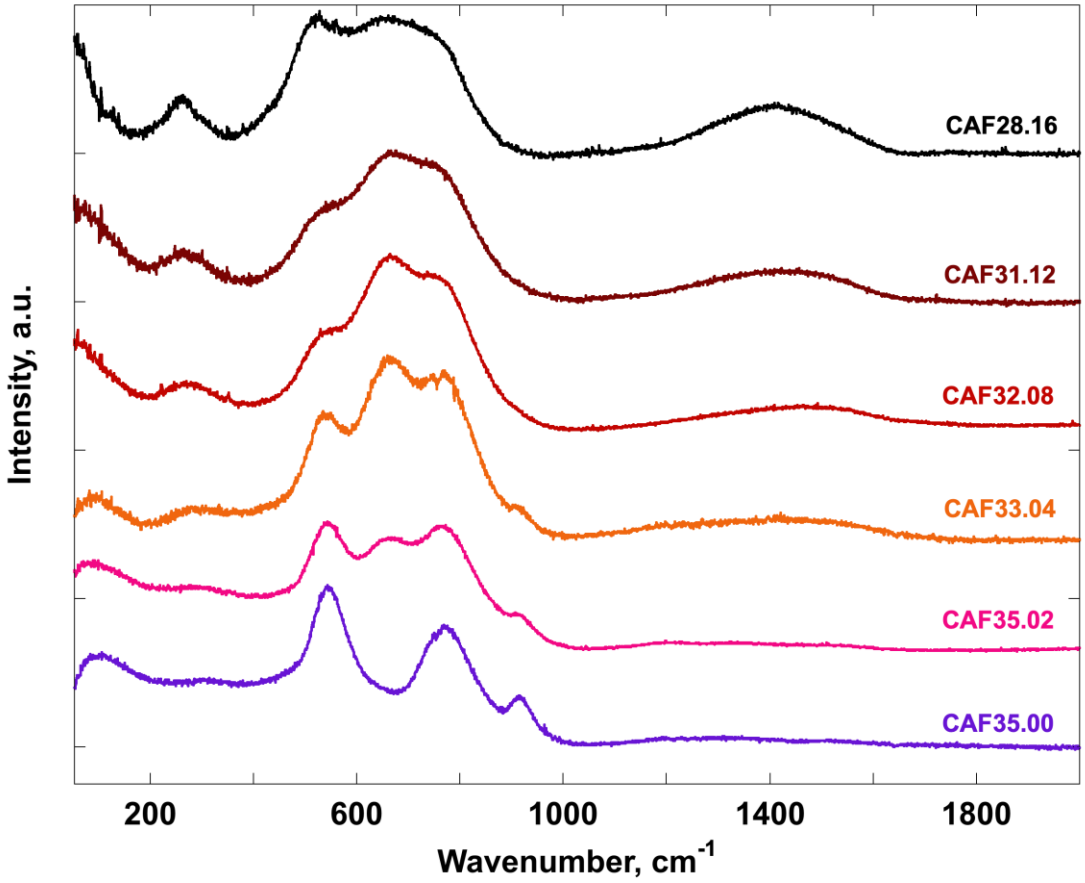

Figure 2. *Unpolarized Raman spectra of CAF glasses. Vertical lines high-lights the changes occurring by increasing the iron content.*

- The intermediate frequency region: 200-1100 cm^{-1}

In CAF35.00 – the iron free calcium aluminate – a small band is visible around 305 cm^{-1}. This band can be attributed to vibrations of alkaline or alkaline earth elements [63]. This band becomes more intense and shifts to lower frequencies with the addition of iron, starting from 2 mol % of Fe_2O_3 at 293 cm^{-1} and going down to 261 cm^{-1} for 16 mol % of iron. The band at 545 cm^{-1} is due to the presence of Al—O—Al bridges [34], [44], [68]. It becomes wider and shifts to lower frequencies up to 518cm^{-1} with 16 mol % of Fe_2O_3.

A distinct difference between the spectra of iron-bearing and iron-free samples is the depolarized band around 655 cm^{-1} in the aluminate vibration region. This band grows in intensity and stays constant in frequency with increasing iron content. According to Mysen et al. [14], [15] this band can be attributed to the presence of iron. This observation is well correlated with results from the XANES spectroscopy at the Fe K-edge which shows that iron is only present in the trivalent oxidation state and a four and/or five-fold coordination.

The band at 768 cm^{-1} was assigned to Al—O stretching [34], [68], whereas the band at 910 cm^{-1} corresponds to the presence of orthoborate triangular units formed at low concentrations of B_2O_3 [32], [37], [69] [70]. This band is still visible up to 4 mol % of Fe_2O_3 and then vanishes under the envelope formed between 400 and 900 cm^{1}.

- The high frequency region: 1100-1800 cm^{-1}

This region is occupied by a large envelope that increases in intensity with the addition of iron. The bands in the high frequency range were assigned by Kamitsos et al. [71], [72] to the $B\text{-}O^-$ bonds of large borate groups. The band increases in intensity and shifts to a lower frequency due to the presence of iron that modifies the distribution of BO_3 and BO_4 units. The deconvolution of this envelope will be detailed below.

3.3 Viscosity at low temperature and glass transition temperature

The results of the viscosity measurements on the CAF series are listed in Table 3, and are plotted in Figure 3 as a function of the reciprocal temperature. We also added values for iron-free $C_{12}A_7$ and CAF35.00 glasses from El Hayek et al. [37], without and with boron respectively, for comparison. Viscosity measurements are made up to 8 mole % of Fe_2O_3 as it was not possible to obtain glasses that are large enough to produce cylindrical samples with higher Fe contents. For higher concentrations than 8% mole of Fe_2O_3, a few grams of each composition were quenched in order to obtain glasses to measure their density, Raman spectroscopy, and Tg. Viscosity curves show a non-Arrhenian behavior of the supercooled liquids along the 4 orders of magnitude of the measurements which is in agreement with previous data on C12A7, which corresponds to a very fragile glass composition [33], [34].

The addition of boron – shown by the curves corresponding to $C_{12}A_7$ and CAF35.00 – decreases the viscosity by breaking the aluminate network [37]. The change in the slope with boron content is probably due to a change in the coordination number of boron with temperature according to Cormier et al. [73]. Iron addition produces a non-linear decrease of viscosity with increasing iron content. As the concentration of iron increases up to 8 mol%, the viscosity always shows a non-Arrhenian behavior along the 4 order of magnitude measuring range and shows a decrease respectively of 0.5, 1 and 2.5 orders of magnitude for 2, 4 and 8% Fe_2O_3 in mole percent. Using the data from the viscosity measurements, it is possible to determine the parameters of Tamman-Vogel-Flucher (TVF) equation used to interpolate viscosity data: $\log \eta = A + B/(T - T_1)$, where A, B and T_1 are empirical parameters. The TVF parameters are given in Table 4 with the glass transition temperature, Tg_η taken at a constant viscosity of 10^{12} Pa.s.

Table 3. *Viscosity measurements in log Pa.s at different temperature in Kelvin, performed with the creep apparatus on CAF glasses.*

CAF37.00		CAF35.00		CAF35.02		CAF33.04		CAF32.08	
T	log η	T	log η	T	log η	T	log η	T	log η
1181.2	8.51	1037.6	9.84	1137.7	8.90	1120.5	8.50	1095.6	8.39
1171.7	8.92	1116.1	10.55	1126.1	9.40	1115.3	8.80	1083.4	8.98
1162.2	9.30	1106.7	10.94	1121.1	9.68	1103.4	9.30	1073.3	9.51
1153.6	9.68	1097.5	11.29	1116.1	9.91	1094.3	9.79	1069.6	9.71
1144.4	10.16	1084.6	11.59	1105.0	10.40	1085.1	10.30	1062.8	10.05
1136.8	10.53	1083.1	11.87	1102.8	10.70	1075.6	10.80	1059.0	10.25
1126.3	11.16	1077.2	12.17	1093.8	10.86	1073.4	10.93	1054.5	10.55
1116.3	11.81			1091.7	11.03	1062.3	11.45	1044.6	11.08
1106.1	12.32			1082.8	11.48	1053.2	11.89	1038.3	11.50
				1075.3	11.82	1048.2	12.20	1026.6	12.20
				1063.8	13.40				

Table 4. *A, B and T_1 parameters calculated from the TVF fit on the low-temperature viscosity data (Table 3) and glass transition temperature T_g calculated for log=12 log Pa.s. The input temperatures and viscosities are in Kelvin and Pa·s respectively.*

	CAF37.00	CAF35.00	CAF35.02	CAF33.04	CAF32.08
A	-9.9075	-2.8493	-17.593	-19.755	-4.194
B	7931.7	5110.5	16298.0	17764.0	4406.7
T_1	749.6	735.0	500.2	493.0	754.2
Tg_η	1111.6	1079.2	1072.2	1051.9	1029.4

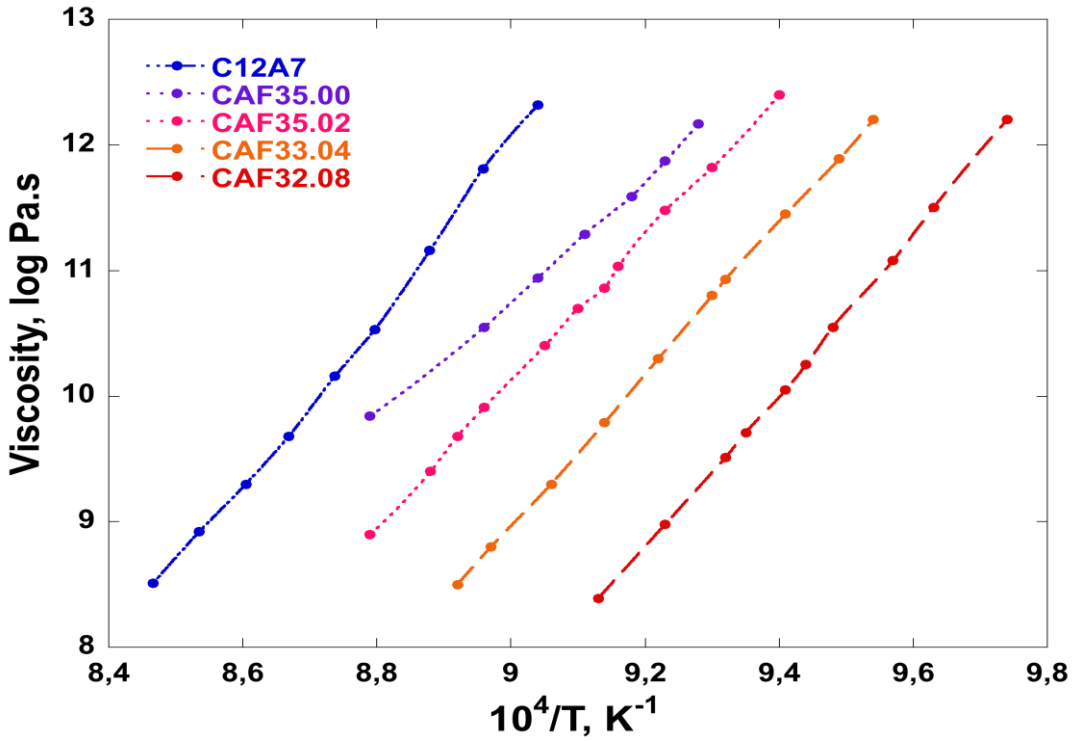

Figure 3. *Viscosity of glasses plotted as a function of the reciprocal temperature. C12A1 is calcium aluminate, the starting composition, CAF35.00, the iron free boroaluminate glass, and others CAFX.Y, with Y the iron content (lines are guides for the eyes).*

The viscosity and DSC measurements show that the addition of iron in aluminate glasses produces an important decrease of Tg_η. It becomes larger with iron content (Figure 4). This

effect observed at low temperature is of a larger magnitude than the one already known at high temperature on sodium iron aluminosilicate melt [16], [17], [74].

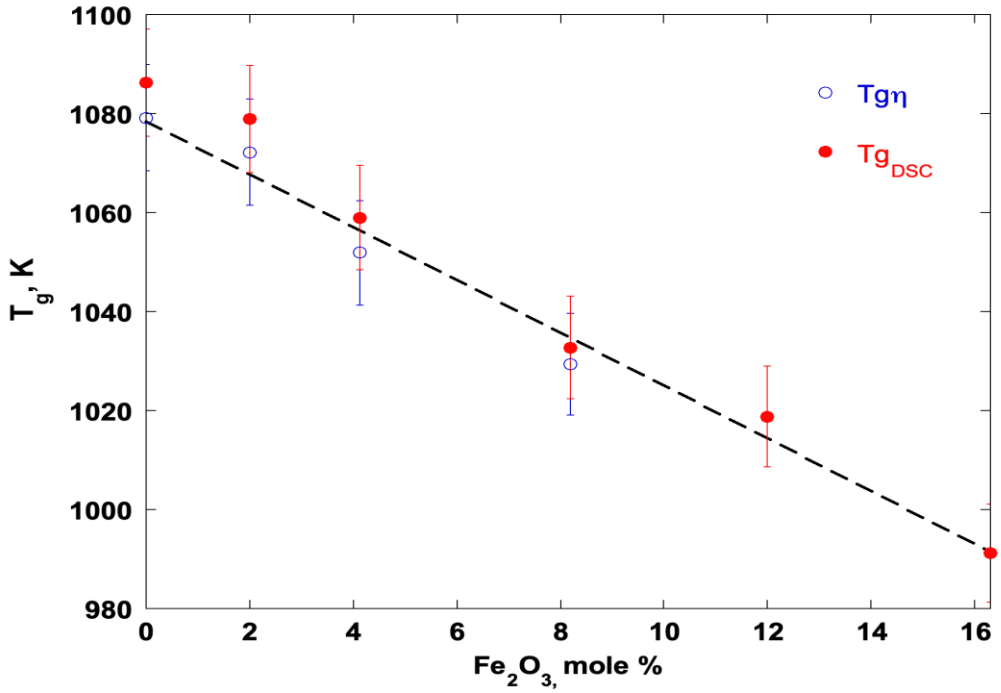

Figure 4. *Glass transition temperature as a function of Fe_2O_3, determine from the TVF parameter and measure with DSC experiment with and heating rate of 10K/min.*

4. Discussion

4.1 Effect of ferric iron on the density and molar volume of aluminate glass

XANES spectroscopy at the Fe K-edge show a strong pre-edge peak, characteristic of the prevalent presence of Fe^{3+} in tetrahedral coordination [23], [30], [32], [51], [53]. This ferric iron in four-fold coordination can link easily with aluminum in the aluminate network. Both cations will play the role of a network former in these invert glasses.

As a first consequence of the presence of $^{[4]}Fe^{3+}$ in the CAF glasses, an increase of the density is observed when adding Fe_2O_3 to the glass (Figure 1d). Indeed, two factors contribute to the increase of density: the molecular weight of Fe_2O_3, which is higher than Al_2O_3 and the iron coordination which is mainly in $^{[4]}Fe^{3+}$ form in our compositions. This leads to the contraction of the network causing a decrease of its volume [14]. In summary, the inverse relationship between the molecular weight and the volume of the network induces a net increase of the density. The molar volume of the alumina glasses increases from 24.5 cm^3 to 26.5 cm^3 with the addition of 16 moles of Fe_2O_3. The increase can be simply explained by the fact that the $^{[4]}Fe^{3+}$-O distance is larger than Al^{3+}-O distance, respectively 1.86Å for $^{[4]}Fe^{3+}$-O distance from recent neutron measurements [75] and 1.76Å for Al^{3+}-O distance [76], [36].

4.2 Macroscopic effect of ferric iron on aluminate glass

Figure 4 shows that Tg calculated with the TVF equation or from DSC measurements decrease as a function of Fe_2O_3 content. The same trend is clearly visible between Tg_η and Tg_{DSC}. Tg_{DSC} is always higher 10±5K than Tg_η and in line with Tequi et al. [77]. While doubling the concentration of iron, Figure 4 shows a drop of T_g by ~30K. With 4% of Fe_2O_3, iron is in 3+ and 4-fold

coordination as shown in Figure 1c. For higher iron contents, the average iron coordination smoothly increases to 5-fold for 16 mole percent of Fe_2O_3 (CAF28.16 composition). These observations are also in good agreement with the fact that the slope of the viscosity curves for CAF35.02, CAF33.04 and CAF32.08 are similar. This implies that iron plays the same role and stays in $^{[4]}Fe^{3+}$ in agreement with XANES at the Fe K-edge and the Raman spectra which shows a Fe^{3+} band at 650cm^{-1}. We can propose the assumption that the decrease of Tg for CAF31.12 and CAF28.16 results from a slow increase in the iron coordination from 4 to 5. However, some important points must be considered to explain the evolution of T_g and the viscosity:

- two network formers are in competition in the glass network: aluminum and Fe^{3+}.
- The bond energy of iron (Fe—O= 409 kJ/mol) is lower than aluminum (Al—O= 512 kJ/mol)
- $^{[4]}Fe^{3+}$ can easily replace aluminum in a tetrahedral species. The incorporation of iron in the aluminate network fragilizes the matrix thus leading to a decrease of the viscosity and the glass transition temperature. The increase of Fe average coordination number could also have an impact on the viscosity and Tg. However, more experimental data are needed to explain the influence of the average coordination number on the evolution of physical properties.

4.3 Mechanical introduction of iron in the tetrahedral network of glasses

The structure of CAF35.00 (the base calcium aluminate glass with 2 mol% B_2O_3) consists of a tridimensional network of AlO_4 tetrahedral units as highlighted by the presence of two bands around 550 et 780 cm^{-1} in the Raman spectra (the aluminate region) and a minor amount of B^{3+} in 3-fold coordination [37]. When increasing the iron content in CAF glasses, a new band is observed in the intermediate frequency region, around 650 cm^{-1}. XANES spectra of CAF glasses already confirmed the presence of Fe^{3+} in four-fold coordination (Figure 1a,b,c).

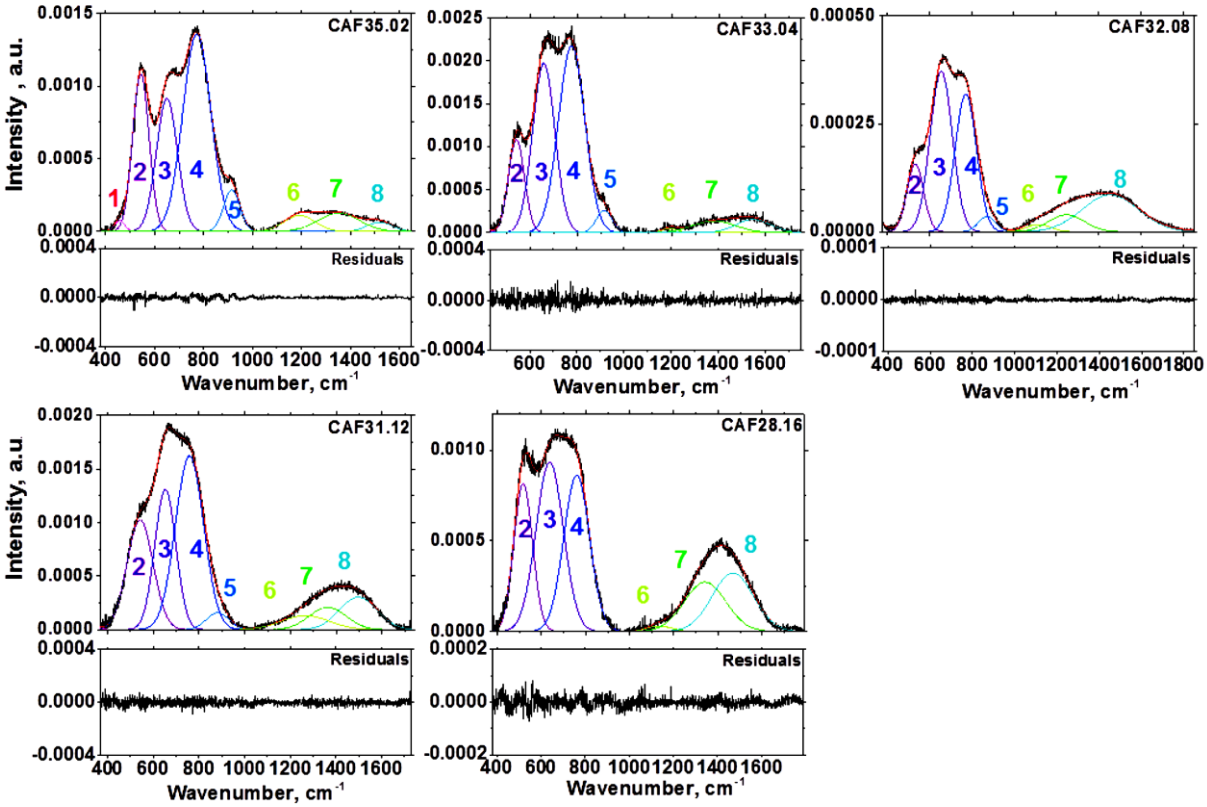

Figure 5. *Deconvoluted Raman spectra of the respective samples.*

The Raman spectra of iron-bearing silicate glasses show a strong band near 970 cm^{-1} – within the silicate region – that grows with the addition of iron (Figure 5). Mysen et al. [14], [15] assigned this band to a 4-fold coordinated Fe^{3+} interconnected with the silicate framework. This interpretation is going along with the study of Virgo et al. [78], [79], [80], [81] for the spectra of quenched melts (glasses) in the Na_2O-SiO_2-Fe_2O_3-FeO system where Fe^{3+} is in a tetrahedral coordination. In fact, this band is more accurately attributed to the vibration mode of Si—O in the Si—O—$^{[4]}Fe^{3+}$ link. In an analogous manner, the similarity of the ionic charge between Fe^{3+} and Al^{3+} enables iron to easily substitute aluminum in the glass framework, hence allowing the appearance of a Raman band in the aluminate region. The band around 650 cm^{-1} can then be attributed to the vibration mode of Al^{3+}—O in the Al^{3+}—O—$^{[4]}Fe^{3+}$ link (Figure 6).

Following the comparison between ferrosilicate and ferroaluminate glasses, it seems that the band attributed to the presence of iron in the matrix is a network dependent peak (Figure 6). Consequently, its frequency changes according to the tridimensional network formed in the glass.

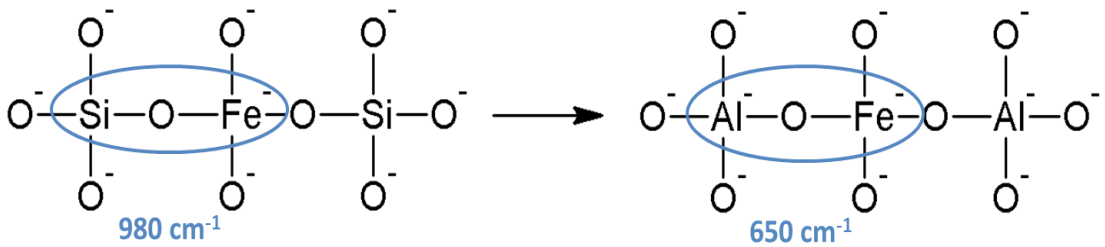

Figure 6. *Schematic explanation for iron band vibration in silicate and aluminate network.*

In the high frequency region, the intensity of the envelope between 1100 cm^{-1} and 1800 cm^{-1} – associated to borate species – tends to increase in intensity with the addition of iron. In order to get detailed information about the structure, and the different borate species present in the glasses, the full deconvolution of both intermediate and high-frequency regions in Raman spectra has been carried out by using up to 8 components (listed in table 4), representing the different vibration units (Figure 5). The frequency, width and area of each Gaussian band are given in table 5.

At low iron concentrations (CAF35.02 glass), a band around 450 cm^{-1} appears which can be assigned to BO_4 isolated units [69]. This band disappears under the large envelope in the intermediate frequency range when the concentration of iron increases. The high frequency region of the Raman spectra is characterized by bands involving the vibration of BO_3 and BO_4 units. This high frequency envelope was fitted using three bands (6 to 8 in Figure 5). The band around 1190 cm^{-1} is associated with the vibration of two Al in four-fold coordination linked to a BO_3 unit [69]. Bunker et al. [70] found that the bands around 1350 cm^{-1} and 1520 cm^{-1} are due to $BØ_2O^-$ (Ø= bridging oxygen) triangle units linked to $BØ_4$-units and $BØ_2O$-triangles linked to other BO_3 units respectively. These two contributions are denoted A4 and A3 respectively. It seems that the intensity of the A4 band, rises with the addition of iron. Since the proportion of BO_4 units in the glasses is directly related to the area of the A4 band then, the concentration of these units should increase with the addition of iron.

Table 5. *Deconvoluted bands obtained from the fits of the Raman spectra: U_x, W_x, $Area_x$ correspond to the frequency in cm^{-1}, FWHM in cm^{-1}, the area in a.u., with x indicating the frequency of each band, respectively. Raman spectra deconvolution parameters for the CAF35.00 are already published in El Hayek et al. (2017).*

Bands	CAF35.02	CAF33.04	CAF32.08	CAF31.12	CAF28.16
U_{450}	457.16	-	-	-	-
U_{540}	543.78	540.41	533.61	541.94	516.29
U_{650}	650.35	656.29	656.77	652.38	636.40
U_{770}	772.44	774.68	772.82	758.22	758.94
U_{910}	914.91	913.77	873.51	880.32	-
U_{1190}	1192.27	1192.36	1115.73	1265.01	1135.14
U_{1350}	1352.29	1382.64	1248.6	1362.76	1341.29
U_{1510}	1518.49	1540.96	1456.19	1495.32	1466.89
W_{450}	49.37	-	-	-	-
W_{540}	78.83	79.93	93.19	134.73	99.29
W_{650}	101.17	110.42	122.74	108.51	145.93
W_{770}	134.96	131.67	119.19	145.48	138.30
W_{910}	78.66	78.56	97.13	116.63	-
W_{1190}	149.71	73.75	137.21	248.62	127.78
W_{1350}	197.14	214.96	202.88	192.48	220.71
W_{1510}	121.49	174.71	314.39	194.74	219.70
A_{450}	0.004	-	-	-	-
A_{540}	0.091	0.091	0.015	0.147	0.086
A_{650}	0.098	0.232	0.048	0.151	0.145
A_{770}	0.196	0.304	0.040	0.251	0.127
A_{910}	0.024	0.022	0.004	0.019	-
A_{1190}	0.018	0.004	0.002	0.035	0.004
A_{1350}	0.026	0.031	0.035	0.043	0.064
A_{1510}	0.008	0.029	0.029	0.063	0.075
N_{4Raman}	0.536	0.484	0.530	0.305	0.448

It is possible to determine the fraction of boron in BO_4 units, N_{4Raman} (N4R), i.e. N4R= $BO_4/[BO_4+BO_3]$, from the total area of the different bands involving BO_4 species and the total area of bands associated to borate species

In our work, the resolved bands involving vibration of BO_3 species are the bands that correspond to the vibration of the orthoborate group around 910 cm^{-1} (band 5 in Figure 4), the band around 1190 cm^{-1} assigned to the vibration of AlO_4^-—BO_3—AlO_4^- (band 6 in Figure 4), and the one around 1520 cm^{-1} associated with the vibration of $BØ_2O^-$ — BO_3 (band 8 in Figure 4). The bands involving vibrations of BO_4 species are those attributed to BO_4 isolated units around 450 cm^{-1} and the second one around 1350 cm^{-1} associated with the vibration of $BØ_2O^-$ — BO_4 (bands 1 and 7, respectively).

$$N_{4R} = \frac{A_{450} + A_{1350}}{A_{450} + A_{910} + A_{1190} + A_{1350} + A_{1520}} = \frac{A_{450} + A_{1350}}{A_{\Sigma B_2 O_3}} \quad (2)$$

A_x, where A corresponds to the integrated area and x to the frequency of each band.

N_{4Raman} values are reported in table 4. Apparently, this fraction remains nearly constant as observed by Cochain et al. [32] for borosilicate glasses, except for CAF31.12 glass. It seems that the fraction of boron in tetrahedral coordination (N_4) is independent of iron content. Although N_{4R} remains nearly constant, Raman data show considerable changes in BO_3 and BO_4 structural environment with the addition of iron (Figure 5). The increase of $BØ_2O^-$— BO_4 entities

observed when increasing the concentration of Fe_2O_3 implies a rearrangement of medium range order around the BO_4 tetrahedra.

The macroscopic properties are altered by the addition of iron as a direct consequence of the structure modifications.

4.4 Optical basicity of CAF glasses.

Duffy and Ingram [82] developed the optical basicity concept in order to determine the acido-basicity properties of mixtures containing large numbers of oxides. Usually, the oxygen behaves as a Lewis base and the metal ions behave as a Lewis acid [21]. It is possible to calculate the so-called theoretical optical basicity of a multi-oxide glass on the basis of the equation proposed by Duffy and Ingram [82] as the average basicity of all oxides present in the glass. Ottonello optical basicity values were used to calculate the theoretical optical basicity of CAF glasses [20]. The optical basicity of each CAF glass was calculated as follows:

$$\Lambda_g = \frac{\sum_{i=1}^{4} n_i \times O_i}{O_{total}} \quad (3)$$

Where Λ_g is the optical basicity of the glass, n_i is the molar percent of each oxide present in the glass, O_i is the number of oxygen atoms composing each oxide, O_{total} is the number of all oxygen atoms present in the glass.

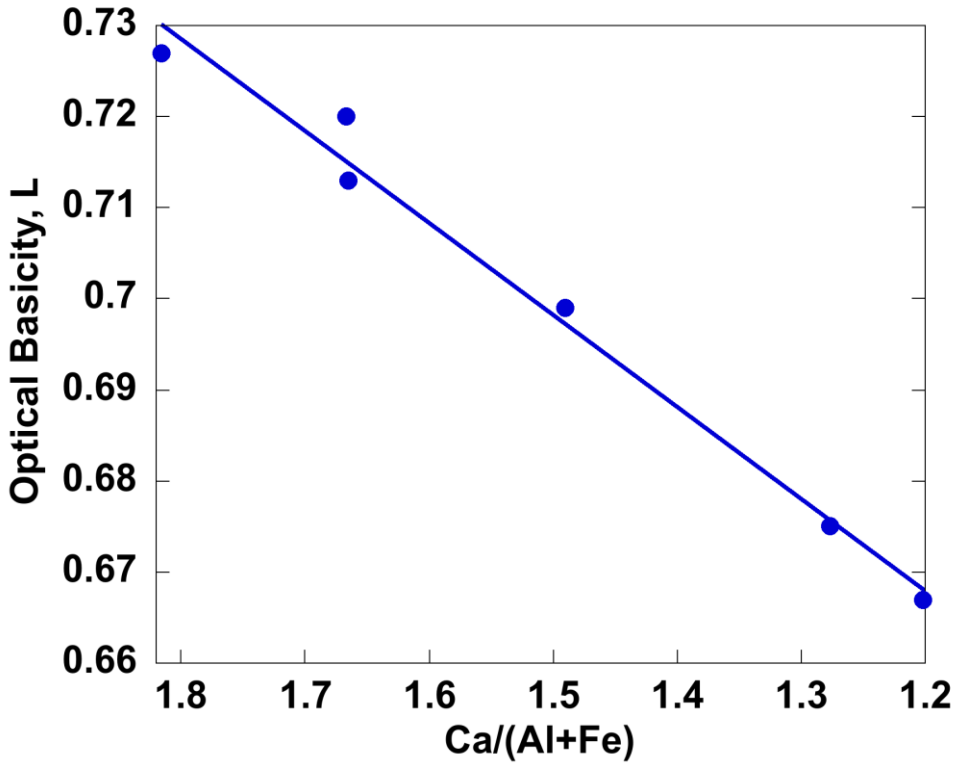

Figure 7. *The drop of the theoretical optical basicity for CAF glasses by increasing the content of iron.*

In Figure 7, the theoretical optical basicity, Λ, is plotted *versus* Ca/(Al+Fe). Obviously, the decrease of optical basicity is mainly associated with the change in the Ca/(Al+Fe) ratio.

4.5 Viscosity of CAF(B) glasses and melts

To better discuss the impact on clinkering, the viscosity was plotted as a function of iron content and temperature and is presented in Figure 8. Although the measurements were performed

on glass samples at moderate temperatures, a qualitative prediction at high temperature is possible as the measurements were performed in the region of a supercooled liquid (above T_g). When increasing the Fe_2O_3 level from 0 to 8 mol% in the supercooled liquid, the viscosity is lowered by almost 3 orders of magnitude. The liquid phase in iron bearing clinker systems is therefore much more fluid than in low iron calcium aluminate systems. It is obvious that this decrease of viscosity is one of the key properties to increase the burnability of a given raw mix.

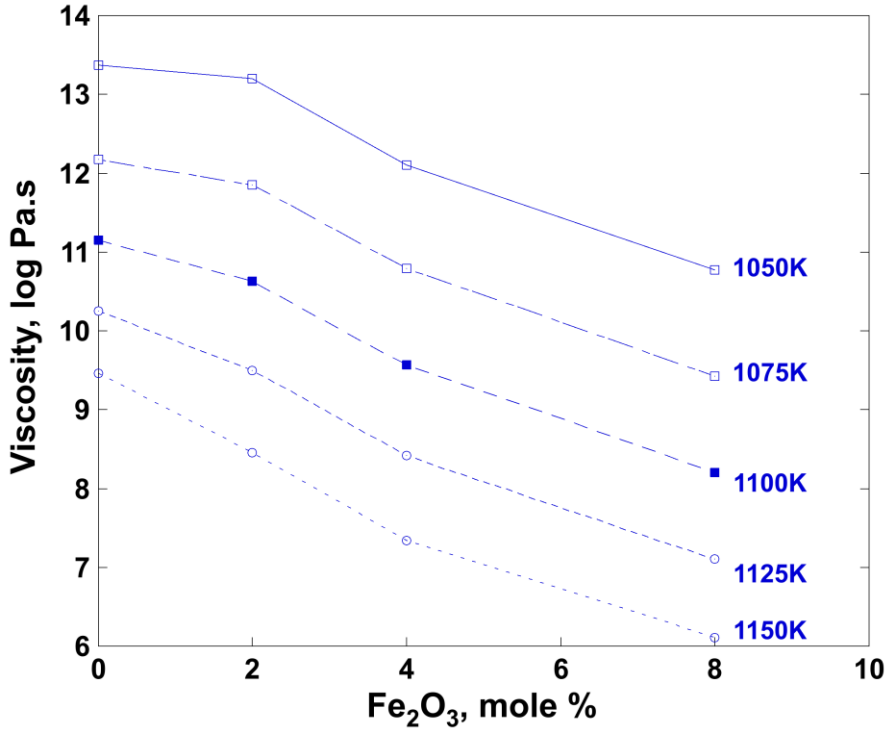

Figure 8. *Viscosity as a function of iron composition at different temperatures (lines are guides for the eyes).*

The diffusion of the elements in the liquid is enhanced and the formation of nodules in the rotary kiln is favored. In addition, in BYF type cements, the presence of the liquid phase triggers the formation of Fe-bearing ye'elimite [5], [7] with better hydration properties. In BYF and OPC clinker, the presence of the liquid phase leads to the formation of nodules in the clinkering process that are important for an optimum cooling process in the grate coolers. In addition, in OPC clinkers the presence of the liquid enhances the reaction kinetics of the $C+C_2S=C_3S$ Alite formation reaction via diffusion of Ca through the liquids phase [10] which improves the burnability. Due to the lower viscosity, the liquid phase dispatches much faster in the complete raw mix inside the kiln and therefore increases the homogeneity and the process stability. Last but not least, the presence of a liquid with lower viscosity improves the coating formation at the surface of the refractories which is important to increase their lifetime. However, a drawback may be that the overall clinkering process is more difficult to control and overburning may be observed more frequently.

5. Conclusion

Iron speciation has a strong influence on melt structure and physical properties. For CAF glasses, Raman and XANES spectra show the presence of mainly iron (3+) more precisely in 4-fold coordination. The wet chemical analysis has shown that the Fe^{3+}/Fe_{tot} ratio is constant along the CAF join. This behavior indicates that ferric iron is stabilized by the presence of network modifier cations like Ca^{2+} and prefers the tetrahedral coordination when sufficient alkalis or alkaline earth elements are available for charge balance. Therefore, ferric ion behaves as a structural analogous to Al^{3+}. At higher Fe contents, a part of the trivalent iron could be

stabilized in higher coordination numbers since the $CaO/(Al_2O_3+Fe_2O_3)$ molar ratio decreases. As a result, both glass transition temperature and viscosity at low temperature decrease with the addition of iron. Furthermore, it is important to point out that the network forming ability of iron is weaker than aluminum.

Beside the effect on physical properties, we observed an increase in BO_4 tetrahedral units with the addition of Fe_2O_3. Only then, calcium starts to play the role of a network modifier in order to create non-bridging oxygen needed for the formation of BO_4 units. The effect of iron on B_2O_3 structural units is not well known. Further experimental data will be required to understand this interaction.

Due to the structural variations in the glass / supercooled liquidus with the addition of Fe_2O_3, a lowering of the viscosity of almost three order of magnitudes is observed. This lower viscosity has a strong impact on the clinkering process. The melt becomes more fluid, favors the formation of nodules and therefore increases the burnability of a given raw mix. In the case of BYF type cements, the formation of Fe-bearing ye'elimite should be favored.

The newly acquired structural data can now be linked to reactivity considerations of the glassy phase. Further experimental work is needed to study the hydration behavior of these BYF type iron-bearing glasses with and without the presence of boron.

Data availability statement

The data that support the findings of this study are available from the corresponding author upon reasonable request.

Underlying and related material

Correspondence and requests should be addressed to corresponding author.

Author contributions

R. El Hayek: Investigation, Formal analysis, Writing - Original Draft, **F Ferrey:** funding, review & editing **A. Pisch:** funding, review & editing, **M.R Cicconi:** XANES measurements and treatment. Writing - Review & Editing **D. Vantelon:** in charge of the beamline experiment **D.R. Neuville:** Conceptualization, Methodology, Writing - Review & Editing, Project administration, Funding acquisition, Resources.

Competing interests

The authors declare that they have no competing interests.

Funding

Lafarge funding and CIFRE support.

Acknowledgement

We acknowledge SOLEIL for provision of synchrotron radiation facilities. OXYMORE funding from Ile de France and ANR Dystras to support the Multi HT96 LINE TGA-DTA/DSC Setaram.

References

[1] IEA (2021), *Global Energy Review 2021*, IEA, Paris https://www.iea.org/reports/global-energy-review-2021

[2] S. Kucharczyk, M. Zajac, C. Stabler, R.M. Thomsen, M. Ben Haha, J. Skibsted, J. Deja Structure and reactivity of synthetic $CaO-Al_2O_3-SiO_2$ glasses, Cem. Concr. Res. 120 (2019) 77–91. DOI:10.1016/j.cemconres.2019.03.004

[3] E. Gartner, Industrially interesting approches to “low-CO2” cements, Cem. Concr. Res. 34 (2004) 1489-1498. DOI:10.1016/j.cemconres.2004.01.021

[4] M. Ben Haha, F. Winnefeld & A. Pisch. Advances in understanding ye'elimite-rich cements. Cement and Concrete Research, 123 (2019) 105778. DOI:10.1016/j.cemconres.2019.105778

[5] F. Bullerjahn, M. Zajac, M. Ben Haha, & K.L. Scrivener. Factors influencing the hydration kinetics of ye'elimite; effect of mayenite. Cement and Concrete Research, 116 (2019) 113-119. DOI:10.1016/j.cemconres.2018.10.026

[6] Y. Huang, Y. Pei, J. Qian, X. Gao, J. Liang, G. Duan, P. Zhao, L. Lu, X. Cheng (2020). Bauxite free iron rich calcium sulfoaluminate cement: Preparation, hydration and properties. Construction and Building Materials, 249 (2020) 118774. DOI:10.1016/j.conbuildmat.2020.118774

[7] F. Bullerjahn, T. Scholten, K.L. Scrivener, M.B. Haha, A. Wolter, A. (2020). Formation, composition and stability of ye'elimite and iron-bearing solid solutions. Cement and Concrete Research, 131, 106009. DOI:10.1016/j.cemconres.2020.106009

[8] H. Liu, W. Chen, R. Pan, Z. Shan, A. Qiao, J.W. Drewitt, L. Hennet, S. Jahn, D.P. Langstaff, G.A. Chass, H. Tao, Y.Z. Yue, G.N. Greaves. From Molten calcium aluminates through phase transitions to cement phases. Adv. Sci., 7 (2020) 1902209. DOI: 10.1002/advs.201902209

[9] F.M. Lea, T.W. Parker, I—Investigations on a portion of the quaternary system CaO-Al2O3-SiO2-Fe2O3: The quaternary system CaO—2CaO.SiO2—5CaO.3Al2O3-4 CaO.Al2O3.Fe2O3 Philosophical Transactions of the Royal Society of London. Series A, Mathematical and Physical Sciences, 234 (731) (1934) 1-41.

[10] H.F.W. Taylor, Cement chemistry, second edition, Thomas Telford, 1997, 460 pp.

[11] T.I. Barry, F.P. Glasser. Calculations of Portland cement clinkering reactions. Advances in cement research, 12(1) (2000)19-28.doi :10.1680/adcr.2000.12.1.19

[12] V.V. Timashev, 7th ICCC conference, Vol. 1 (1980) I-3-1

[13] Yu.M. Butt, V.V. Timashev, A.P. Osokin, 6th ICCC conference, Vol.1 (1976) 132

[14] B.O. Mysen, D. Virgo, F.A. Seifert. Redox equilibria of iron in alkaline earth silicate melts: relationships between melt structure, oxygen fugacity, temperature and properties of iron-bearing silicate liquids. Amer. Mineral., 69 (1984) 834-848.

[15] B.O. Mysen, D. Virgo, E.R. Neumann, F.A. Seifert. Redox equilibria and the structural states of ferric and ferrous iron in melts in the system CaO-MgO-Al2O3-FeO: relationships between redox equilibria, melt structure and liquidus phase equilibria. Am. Mineral., 70 (1985) 317-331.

[16] B.O. Mysen, D. Virgo, C.M. Scarfe, D.J. Cronin. Viscosity and structure of iron and aluminum bearing calcium melts at 1atm. Am. Mineral., 70 (1985) 487-498.

[17] D.B. Dingwell, D. Virgo. Viscosities of melts in the Na2O-FeO-Fe2O3-SiO2 system and factors controlling relative viscosities of fully polymerized silicate melts. Geochim. Cosmochim. Acta, 52 (1988) 395-403. DOI: 10.1016/0016-7037(88)90095-6

[18] V.C. Kress, I.S.E Carmichael. Stoichiometry of the iron oxidation reaction in silicate melts. Am. Mineral., 73 (1988) 1267–1274.

[19] V.C. Kress, I.S.E. Carmichael. The compressibility of silicate liquids containing Fe2O3 and the effect of composition, temperature, oxygen fugacity and pressure on their redox states. Contrib. Min. Petrol., 108 (1991) 82–92.

[20] G. Ottonello, R. Moretti, L. Marini, M.V. Zuccholini. Oxidation state of iron in silicate glasses and melts: A thermochemical model. Chem. Geol., 174 (2001) 157-179.

[21] Moretti R. and Neuville D.R. (2021) Redox equilibria: from basic concepts to the magmatic realm. AGU Geophysical Monography Series eds Moretti and Neuville – DOI : 10.1002/9781119473206.ch1
[22] G.B. Cook, R.F. Cooper, T. Wu. Chemical diffusion and crystalline nucleation during oxidation of ferrous iron-bearing magnesium aluminosilicate glass. J. Non-cryst. Sol., 120 (1990) 207-222.
[23] V. Magnien, D.R. Neuville, L. Cormier, J. Roux, J.-L. Hazemann, D. De Ligny, S. Pascarelli, O. Pinet, P. Richet P. Kinetics or iron redox reactions in silicate melts: the effect of temperature and alkali cations. Geochim. Cosmochim. Acta., 72 (2008) 2157-2168. DOI: 10.1016/j.gca.2008.02.007
[24] D.S. Goldman, P.K. Gupta. Diffusion-controlled redox kinetics in a glassmelt. J. Amer. Ceram. Soc., 66 (1983) 188-190.
[25] H.D. Schreiber, S.J. Kozak, R.C. Merkel, G.B. Balazs, P.W. Jones, Jr. Redox equilibria and kinetics of iron in a borosilicate glass-forming melt J. Non-Cryst. Sol., 84 (1986) 186-195. DOI: 10.1016/0022-3093(86)90777-5
[26] R.F. Wendlandt. Oxygen diffusion in basalt and andesite melts: experimental results and discussion of chemical versus tracer diffusion. Contrib. Mineral. Petrol., 108 (1991) 463-471.
[27] J.L. Barton, D. Banner, D. Caurant, F. Pincemin. The oxidation of ferrous iron in glass at high temperatures II. Fundamentals of Glass Science and Technology, Bul. Soc. Esp. Ceram., 31(6) (1992) 215-220.
[28] R.F. Cooper, J.B. Fanselow, D.B. Poker. The mechanism of oxidation of a basaltic glass: chemical diffusion of network-modifying cations. Geochim. Cosmochim. Acta, 60 (17) (1996) 3253-3265. DOI: 10.1016/0016-7037(96)00160-3
[29] D.R. Smith, R.F. Cooper. Dynamic oxidation of a Fe2+ bearing calcium-magnesium-aluminosilicate glass: the effect of molecular structure on chemical diffusion and reaction morphology. J. Non-Cryst. Solids, 278 (2000) 145-163. DOI: 10.1016/S0022-3093(00)00323-9
[30] V. Magnien, D.R. Neuville, L. Cormier, B.O. Mysen, P. Richet. Kinetics of iron oxidation in silicate melts: a preliminary XANES study., Chem. Geol., 213 (2004) 253-265. doi:10.1016/j.chemgeo.2004.08.047
[31] V. Magnien, D.R. Neuville, L. Cormier, J. Roux, J.-L. Hazemann, O. Pinet, P. Richet Kinetics or iron redox reactions in silicate liquids: a high-temperature X-ray absorption and Raman spectroscopy study. J. of Nucl. Mater., 352 (2006) 190-195. DOI: 10.1016/j.jnucmat.2006.02.053
[32] B. Cochain, D.R. Neuville, G.S. Henderson, C.A. McCammon, O. Pinet, P. Richet. Effects of the iron content and redox state on the structure of sodium borosilicate glasses: A Raman, Mössbauer and boron k-edge XANES spectroscopy study. J. Am. Ceram. Soc., 95 (2012) 962–971. DOI: 10.1111/j.1551-2916.2011.05020.x
[33] D.R. Neuville, L. Cormier, A.M. Flank, D. de Ligny, J. Roux, P. Lagarde. Environment around Al, Si and Ca in aluminate and aluminosilicate melts by X-ray absorption spectroscopy at high temperature, Am. Mineral. 93 (2008) 228-237. DOI: 10.2138/am.2008.2646
[34] D.R. Neuville, G.S. Henderson, L. Cormier, D. Massiot. The structure of crystals, glasses, and melts along the CaO-Al2O3 join: Results from Raman, Al L- and K-edge X-ray absorption, and 27Al NMR spectroscopy. Am. Mineral. 95(10) (2010) 1580–1589. DOI: 10.2138/am.2010.3465
[35] M. Licheron, V. Montouilout, F. Millot, D.R. Neuville. Raman and 27Al NMR structure investigations of aluminate glasses: (1-x)Al2O3-xMO, with M=Ca,Sr, Ba and 0.5<x<0.75. J. Non-Cryst. Solids, 357 (2011) 2796-2801. DOI : 10.1016/j.jnoncrysol.2011.03.001
[36] L. Hennet, J.W.E. Drewitt, D.R. Neuville, V. Cristiglio, J. Kozaily, S. Brassamin, D. Zanghi, H.E. Fischer. Neutron diffraction of calcium aluminosilicate glasses and melts. J. of Non-Cryst. Solids. 451 (2016) 89-93. DOI: 10.1016/j.jnoncrysol.2016.05.018
[37] R. El-Hayek, F. Ferey, P. Florian, A. Pisch, D.R. Neuville. Structure and properties of lime aluminoborate glasses and melts. Chem. Geol., 461 (2017) 75-81. DOI: 10.1016/j.chemgeo.2016.11.025

[38] D.R. Neuville, L. Cormier, A.-M. Flank, V. Brios, D. Massiot. Al speciation and Ca environment in calcium aluminosilicate glasses and crystals by Al and Ca K-edge X-ray absorption spectroscopy. Chem. Geol. 213 (2004) 153-163. DOI: 10.1016/j.chemgeo.2004.08.039
[39] D.R. Neuville, L. Cormier, D. Massiot, Al coordination and speciation in calcium aluminosilicate glasses: Effects of composition determined by 27Al MQ-MAS NMR and Raman spectroscopy. Chem. Geol. 229(1-3) (2006) 173–185. : DOI : 10.1016/j.chemgeo.2006.01.019
[40] J.W.E. Drewitt, L. Hennet, A. Zeidler, S. Jahn, P.S. Salmon, D.R. Neuville, H.E. Fischer. Structural transformations on vitrification in the fragile glass forming system CaAl2O4. Physical Review Letters. 109 (23) (2012) 235501-235506. DOI: 10.1103/PhysRevLett.109.235501
[41] M.R. Cicconi, D. de Ligny, T.M. Gallo, D.R. Neuville. Ca Neighbors from XANES spectroscopy: a tool to investigate structure, redox and nucleation processes in silicate glasses, melts and crystals. Am. Mineral., 101 (2016)1232-1235. DOI: 10.2138/am-2016-5663
[42] J.W.E. Drewitt, A.C. Barnes, S. Jahn, S.C. Kohn, M.J. Walter, A. Novikov, D.R. Neuville, H.E. Fischer, L. Hennet. Structure of liquid tri-calcium aluminate. Physical Review B. 95 (2017) 064203-064214. DOI: 10.1103/PhysRevB.95.064203
[43] D.R. Neuville, G.S Henderson, D.B. Dingwell (2022) "Geological melts" Review in Mineralogy and Geochemistry. DOI: 10.2138/rmg.2022.87.03
[44] J. Drewitt, L. Hennet, D.R. Neuville, (2022) The structure of glasses from short distance order to long distance. In Neuville D.R., Henderson G.S, Dingwell D. B. (2022) "Geological melts" Review in Mineralogy and Geochemistry. DOI: 10.2138/rmg.2022.87.02
[45] P.L. Higby, R.J. Ginther, I.D. Aggarwal, E.J. Friebele. Glass-formation and thermal-properties of low-silica calcium aluminosilicate glasses. J. Non-Cryst. Solids 126(3), (1990) 209–215. DOI: 10.1016/0022-3093(90)90821-3
[46] M. García-Maté, I. Santacruz, A. Cuesta, L. León-Reina, M.A. Aranda, I. Baco, V. Morin, G. Walenta, E. Gartner, A.G. de la Torre. Amorphous determination in calcium sulfoaluminate materials by external and internal methods. Advances in Cement Research, 27(7) (2015) 417-423.
[47] A.J. Cuberos, A.G. De la Torre, G. Alvarez-Pinazo, M.C. Martín-Sedeño, K. Schollbach, H. Pöllmann, M.A. Aranda. Active iron-rich belite sulfoaluminate cements: clinkering and hydration. Environmental science & technology, 44(17) (2010) 6855-6862. DOI: 10.1021/es101785n
[48] G. Alvarez-Pinazo, A. Cuesta, M. Garcia-Maté, I. Santacruz, E.R. Losilla, A.G. De la Torre, L. Leon-Reina, M.A. Aranda. Rietveld quantitative phase analysis of Yeelimite-containing cemenets, Cement and Concrete Research, 42 (2012) 960-971 doi:10.1016/j.cemconres.2012.03.018
[49] D. Vantelon, N. Trcera, D. Roy, T. Moreno, D. Mailly, S. Guilet, F. Delmotte, E. Meltchakov, B. Lassalle, P. Lagarde, A.-M. Flank. The LUCIA beamline at SOLEIL. Journal of Synchrotron radiation, 23(2) (2016) 635-640. DOI: 10.1107/S1600577516000746
[50] Henderson, G. S., De Groot, F. M., & Moulton, B. J. (2014). X-ray absorption near-edge structure (XANES) spectroscopy. Reviews in Mineralogy and Geochemistry, 78(1) (2014) 75-138. DOI: 10.2138/rmg.2014.78.3
[51] G. Calas, J. Petiau (1983) Coordinance of iron in oxide glasses through high resolution K-edge spectra : information from pre-edge. Sol. Stat. Com., 48 625-629. DOI:10.1016/0038-1098(83)90530-6
[52] M. Wilke, F. Farges, P.E. Petit, G.E. Brown, Jr., F. Martin. Oxidation state and coordinance of Fe minerals: an Fe K-XANES spectroscopic study. (2001) Am. Mineral., 86 714 –730. DOI: 10.2138/am-2001-5-612
[53] D.R. Neuville, M.R. Cicconi, Losq C. How measure a redox state? Magma Redox Geochemistry. Magma Redox Geochemistry. AGU Geophysical Monography Series eds Moretti and Neuville. – DOI : 10.1002/9781119473206.ch13
[54] Giuli, G., Cicconi, M. R., & Paris, E. (2012). The Fe3+–O distance in synthetic kimzeyite garnet, Ca3Zr2 [Fe2SiO12]. European Journal of Mineralogy, 24(5), 783-790. DOI: 10.1127/0935-1221/2012/0024-2206

[55] Cicconi, M. R., Giuli, G., Ertel-Ingrisch, W., Paris, E., & Dingwell, D. B. (2015). The effect of the [Na/(Na+ K)] ratio on Fe speciation in phonolitic glasses. American Mineralogist, 100(7), 1610-1619. DOI: 10.2138/am-2015-5155
[56] Neuville D.R., G.S. Henderson and D. de Ligny (2014) Advances in Raman Spectroscopy Applied to Earth and Material Sciences. In Henderson G.S, Neuville D.R., Down B. (2014) "Spectroscopic methods in Mineralogy and Material Sciences" Review in Mineralogy and Geochemistry, Vol 78, 509-541. DOI: 10.2138/rmg.2013.78.13
[57] D.R. Neuville. Viscosity, structure and mixing in (Ca, Na) silicate melts. Chem. Geol., 229 (2006) 28-42. DOI: 10.1016/j.chemgeo.2006.01.008
[58] Pereira L., Linard Y., Wadsworth F.B., Vasseur J., Moretti R., Dingwell D.B., Neuville D.R. (2024) non stoichiometric nano-crystallization in magmas: the impact of composition changes on viscosity. Journal of Volcanology and Geothermal Research. 10.1016/j.jvolgeores.2024.108039
[59] F. Farges. Crystal-chemistry of Fe in natural grandidierites: a XAFS spectroscopy study at the Fe K-edge. Phys. Chem. Minerals, 28 (2001) 619–629. DOI: 10.1007/s002690100170
[60] U. Bucheneau, M. Prager, N. Nücker, A.J. Dianoux, N. Ahmad, W.A. Phillips. Low-frequency modes in vitreaous silica, Phys. Rev.B. 34 (1986) 5665-5673. DOI: 10.1103/PhysRevB.34.5665
[61] B. Hehlen, E. Courtens, R. Vacher, A. Yamanka, M. Kataoka, K. Inoue. Hyper-raman scattering observation of the boson peak in vitreous silica. Phys. Rev. 84(23) (2000) 5355–5358. DOI: 10.1103/PhysRevLett.84.5355
[62] B. Hehlen, E. Courtens, A. Yamanka, K. Inoue. Nature of the Boson peak of silica glasses from hyper-Raman scattering. J. Non-Cryst. Solids 307-310 (2002) 87–91. DOI: 10.1016/S0022-3093(02)01444-8
[63] B. Hehlen, D.R. Neuville. Raman response of Network Modifier Cations in alumino-silicate glasses. J. Phys. Chem. B, 119 (2015) 4093-4098. DOI: 10.1021/jp5116299
[64] G. Simon, B. Hehlen, R. Vacher, E. Courtens. Nature of the hyper-Raman active vibrations of Lithium borate glasses. J. Phys. Condens. Matter. 20(15) (2008) 155103 DOI: 10.1088/0953-8984/20/15/155103
[65] D.R. Neuville, P. Courtial, D.B. Dingwell, P. Richet. Thermodynamic and rheological properties of rhyolite and andesite melts.Contrib. Mineral. Petrol., 113 (1993) 571-581.
[66] Sukenaga S., Cicconi M.R., Yamada H., Wakihara T., Ohara K., Shibata H. and Neuville D.R (2024) Iron redox effect on the structure and viscosity of silicate glasses and melts. The Journal of Chemical Physics. DOI: 10.1063/5.0243427
[67] D. Di Genova, R.A. Brooker, H.M. Mader, J.W.E. Drewitt, A. Longo, J. Deubener, D.R. Neuville, S. Fanara, O. Shebanova, S. Anzellini, F. Arzilli, E.C. Bamber, L. Hennet, G. La Spina, N. Miyajima. In situ observation of nanolite growth in volcanic melt: a driving force for explosive eruptions. Sciences Advances. (2020) – DOI : 10.1126/sciadv.abb041
[68] P. McMillan, B. Piriou. Raman spectroscopy of calcium aluminate glasses and crystals. J. Non-Cryst. Solids 55(2) (1983) 221–242. DOI: 10.1016/0022-3093(83)90672-5
[69] B.N. Meera, J. Ramakrishna. Raman spectral studies of borate glasses J. Non-Cryst. Solids 159 (1993) 1–21. DOI: 10.1016/0022-3093(93)91277-A
[70] B.C. Bunker, D.R. Tallant, R.J. Kirkpatrick, G.L. Turner. Multinuclear nuclear magnetic resonance and Raman investigation of sodium borosilicate glass structures. Phys. Chem. Glasses. 31(1) (1990) 30–41.
[71] E.I. Kamitsos, M.A. Karakassides, G.D. Chryssikos. Vibrational study of lithium borate glasses with high Li2O content. Phys. Chem. Glasses. 28(5) (1987) 203–209.
[72] E.I. Kamitsos, M.A. Karakassides, G.D. Chryssikos. Structure of borate glasses. I: Raman study of caesium, rubidium and potassium borate glasses. Phys. Chem. Glasses, 30(6) (1989) 229-234.
[73] L. Cormier, O. Majérus, D. Neuville, G. Calas, Temperature-Induced Structural Modifications Between Alkali Borate Glasses and Melts. Journal of the American Ceramic Society, 89(1) (2006) 13-19. DOI: 10.1111/j.1551-2916.2005.00657.x
[74] D.B. Dingwell. Viscosity-temperature relationships in the system Na2Si2O5-Na4Al2O5. Geochim. Cosmochim. Acta, 50 (1986) 1261-1265. DOI: 10.1016/0016-7037(86)90409-6

[75] Drewitt J.W.E, Barnes, A.C., Jahn S., Brooker R., Hennet L., Neuville D.R., Fisher H.E. (2023) Direct measurement of iron coordination in levitated liquid FeAl2O4 using neutron diffraction with isotope substitution. Philosophical Transaction of the Royal Society A. https://doi.org/10.1098/rsta.2022.0351
[76] Cormier L., Neuville D.R. and G. Calas (2000) Structure and properties of low-silica calcium aluminosilicate glasses. J. Non-Crystal. Solids.274, 110-114. DOI: 10.1016/S0022-3093(00)00209-X
[77] Téqui C., Robie R.A., Hemingway B.S., Neuville D.R. and Richet P. (1991) Melting and thermodynamic properties of pyrope (Mg3Al2Si3O12). Geochim. Cosmochim. Acta., 55, 1005-1011.DOI: 10.1016/0016-7037(91)90158-2
[78] D. Virgo, B.O. Mysen, I. Kushiro. Anionic constitution of silicate melts quenched at 1 atm from Raman spectroscopy: Implications for the structure of igneous melts. Science, 208 (1980) 1371–1373. DOI: 10.1126/science.208.4450.1371
[79] D. Virgo, B.O. Mysen, F.A. Seifert. Relationship between the oxidation state of iron and structure of silicate melts. Year B. Carnegie. Inst. Wash., 80 (1981) 308- 311.
[80] D. Virgo, B.O. Mysen, P.A. Danckwerth. Redox equilibria and the anionic structure of Na2O.xSiO2-Fe-O melts: effects of oxygen fugacity. Year B. Carnegie. Inst. Wash., 82 (1983) 305-309. DOI : 10.1016/0016-7037(88)90095-6
[81] D. Virgo, B.O. Mysen. The structural state of iron in oxidized vs. reduced glasses at 1 atm: A 57Fe Mössbauer study. Phys. Chem. Min., 12 (1985) 65-76. DOI: 10.1007/BF01046829
[82] J.A. Duffy, M.D. Ingram. An interpretation of glass chemistry in terms of the optical basicity concept. Journal of Non-Crystalline Solids, 21 (1976) 373-410 DOI: 10.1016/0022-3093(76)90027-2